



A new tool to automatise the characterisation of fracture networks from 3D point cloud data

Lionel Bertrand¹, Claire Bossennec², Wan-Chiu Li³, Cédric Borgese³, Bruno Gavazzi¹, Matthis Frey⁵, Yves Géraud⁴, Marc Diraison⁴, and Ingo Sass⁵

¹Enerex, 2 rue du Doyen Marcel Roubault, 54500 Vandoeuvre-lès-Nancy, France

²GFZ German Research Centre for Geosciences, Section 4.8: Geoenergy, Telegrafenberg, 14473 Potsdam, Germany

³Tessael, 615 rue du jardin Botanique, 54600 Villers-lès-Nancy, France

⁴Université de Lorraine, CNRS, GeoRessources, 54000 Nancy, France

⁵Institute of Applied Geosciences, Geothermal Science and Technology, Technische Universität Darmstadt, Schnittspahnstraße 9, 64287 Darmstadt, Germany

Correspondence: Claire Bossennec (claire.bossennec@gfz-potsdam.de)

Abstract. Fracture networks linked to the brittle deformation of rocks are often hosts of fluid flows or geomechanical discontinuities which are important to model for rock mass stability analyses, reservoir assessment or storage capacity evaluation. However, the fractures can be mapped only poorly by subsurface geophysics or borehole imagery. 1D scan lines or 2D maps on outcrops analogues are thus one of the current methods used for the assessemet of the networks, but are very limited regarding the 3D distribution of the fractures. This paper shows the first tests and results for a new automated workflow of fracture properties characterization, using high resolution LiDAR and Photogrammetry data on outcrops. From the obtained 3d point clouds on different objects such as quarries, cliffs or road sides, we reconstruct the outcrop surface in a 3D meshed surface with the help of a Simple and Scalable Surface Reconstruction (SSSR). The fracture planes are automatically detected based on a region-growing segmentation approach based on the spatial distribution of the points. It allows to quickly and effectively extract fracture properties such as orientation, geometry and position in the 3d space, with a possibility for direct 3D density computation without using proxies from 1D or 2D data. This paper present the workflow methodology and the tests on basement rock outcrops of different outcropping quality. We also compare the method with a manual fracture picking tool and a classical 1D scan line methodology on the field. It is a first step to get more precise, automatic, easier and faster modelling workflows on fractured rocks from outcrop analogues data.

1 Introduction

Natural fracture network characterization plays a crucial role for many applications, such as exploration of geothermal resources or of unconventional oil & gas reservoirs, gas storage, civil engineering (Nelson, 2001). However, the fractures are poorly imaged by subsurface acquisition because their size is usually below the resolution of the classic exploration tools, or only with indirect properties (e.g., Slightam, 2014). The only direct way to observe the in-situ fracture network is with borehole imagery, but it can give only very local data at the borehole point, and it is very complex to upscale them to 3D models of



the entire investigated reservoir. Studying fracture networks **on** outcrop analogues is a classic and robust method to assess the fracture properties which may be used as input for flow and geomechanical models.

To model fracture networks, fractures properties such as length, orientation distribution, density, intensity or connectivity have to be measured with a statistical approach (Peacock et al., 2016). Thus statistical scan line (1D) and fracture maps (2D) are now common tools applied to outcrops for their analysis. With the widespread use of technologies such as LiDAR and photogrammetry from Unmanned Aerial Vehicle (UAV) pictures, outcrop studies integrate more and more 3D analysis, in particular for monitoring quarrying, landslides, mining pits or coast lines (Candela, 2011; Bemis et al., 2014; Bonilla-Sierra et al., 2017; Vazaios et al., 2017). However, these tools so far remain underexploited in structural geology. 3D models are often used to make clean orthographic maps or to extrapolate information acquired in 1 or 2D (Seers and Hodgetts, 2016; Martinelli et al., 2020). Only few works on faults and folds detection, fault trace mapping or fault plane rugosity characterization are performed directly on 3D data (Candela, 2011; Micklethwaite et al., 2012; Jacquemyn et al., 2015; Cawood et al., 2017). Several algorithms are available that automatize the mapping of rock discontinuities (Thiele et al., 2017; Prabhakaran et al., 2021), by propagating the fracture trace regarding pixel characteristic similarities or ridge detection followed by vectorisation of the fracture trace. However, very few works in the literature propose ways of automatization of the extraction of fractures as planes in 3D.

Previous investigations on outcrop LiDAR images (Bossennec et al., 2021; Frey et al., 2022b) demonstrated that 3D automatic plane recognition through a Ransac approach that efficiently estimates fracture plane orientations (Schnabel et al., 2007). However, the geometrical features of the identified planes do not adequately fit the ones observed in 2D because the fracture planes are not completely reconstructed (Bossennec et al., 2021). This paper presents a new software tool technology (RECO3D) derived from the Ransac algorithm that reconstructs the fracture planes on a 3D point cloud acquired **on** outcrops. After describing the workflow from data acquisition to processing, results from five outcrops with different outcropping qualities are presented to show the efficiency of the automated fracture recognition. The proposed workflow integrates both LiDAR 3D point cloud analysis and classical structural scan lines carried out in the field to validate the numerical plane reconstruction. After giving some guidelines on the precautions required for this method, this study aims to validate the efficiency of the RECO3D software tool and prove its capacity to quantitatively characterise fracture network properties from 3D point clouds of rock outcrops.

2 Materials and Methods

The RECO3D tool is tested on five basement rocks outcrops scanned with a terrestrial LiDAR. These were selected to represent typical lithologies used as analogous to deep geothermal drilling targets in the West European Rift System (WERS). They all belong to Hercynian basement rocks outcropping at the shoulders of the Limagne Graben in France and in the Odenwald at the shoulders of the Upper Rhine Graben in Germany. The next section briefly resumes the general geological history and data acquisition process on each outcrop, and thereafter the workflow of the LiDAR data processing.



2.1 Geological settings of the selected outcrops

The so-called Hercynian basement rocks originated from the large-scale Variscan orogeny, and outcrops can now be found all over the Europe. In Western Europe, the maximum tectonic activity was roughly between 360 and 300 Ma and led to the formation of several lithological units depending on the original plate, their position and their metamorphism degree during the orogenic collision (Matte, 2001; Nance et al., 2010; Skrzypek et al., 2014; Lardeaux et al., 2014). These rocks are now the basement of the West European large-scale Permian to Cretaceous basins and of the different grabens composing the European Cenozoic Rift System that formed since the late Eocene Epoch (Bourquin et al., 2007; Schumacher, 2002; Ziegler, 1990; Bourgeois et al., 2007). They are now the target of several deep geothermal drilling projects, especially in the Upper Rhine Graben in France and Germany, but also in the other grabens linked to the rift system (Bertrand et al., 2021; Frey et al., 2022a).

The five presented outcrops have been selected to represent both different outcrop properties to test the RECO3D tool, and the lithological units variability through the West European Hercynian basement and their fracture network. The outcrops Combronde and Enval are located at the shoulders of the Limagne graben in the French Massif Central (Figure 1b). They belong both to the so-called Moldanubian unit, which is the now exhumed metamorphic root of the Hercynian orogeny (Skrzypek et al., 2014; Lardeaux et al., 2014). The regional fault pattern is linked to the graben formation and inherited structure reactivation with mostly N and NE trending faults. Enval outcrop is in a dioritic body that belongs to the so called Upper Gneissic Unit (UGU) characterized by magmatic association of acidic to ultramafic rocks, high pressure rocks and migmatites formed by partial melting of pelitic and quartzofeldspathic rocks (Faure et al., 2009). The outcrop is located at the intersection between a N010°E fault with a decametric fault core and a regional scale N080°E fault, and it is also in the extension of the large-scale Aigueperse NE-SW fault (Figure 1b). Combronde outcrop is located in the so called « tuffs anthracifères » unit that is composed of terrigenous and felsic magmatic rocks dated from Late Visean (Bruguier et al., 1998). The outcrop is located near the N-S bordering fault of the basin. The studied area comprises the hanging wall of a local scale fault with an E-W orientation, dipping 85° to the North with a meter thick brecciated and clay-altered fault core. For both of these outcrops the LiDAR acquisition was carried out with a Laser Scanner Focus 3D X330 from Faro© apparatus and the post-acquisition processing was done with the classic workflow of SCENE© software (FARO® SCENE Software, 2021). The acquisition in Enval is composed of three LiDAR scans at 7 m from the outcrop and a 5 m distance between each. For Combronde, three large-view scans were acquired at approximately 12 m horizontal distance from the outcrop and four high-resolution scans at 4.5 m, with a 5 m spacing between the scans. The mean resolution obtained for the final clouds is estimated at 5 mm.

The localization and geologic context of the Odenwald crystalline outcrops are extensively described in Bossennec et al. (2022). Three outcrops are integrated in this study, with varying lithology and structural features (Figure 1c). From South to North, the Tromm pluton is described as a medium- to coarse-grained, orthoclase-rich, biotite-bearing and often reddish granitic-granodioritic pluton. This pluton is affected to the East by the major regional shearing Oetzberg Fault zone, and the investigated outcrop exhibits a fracture pattern with secondary structures associated to the shearing. The second outcrop in

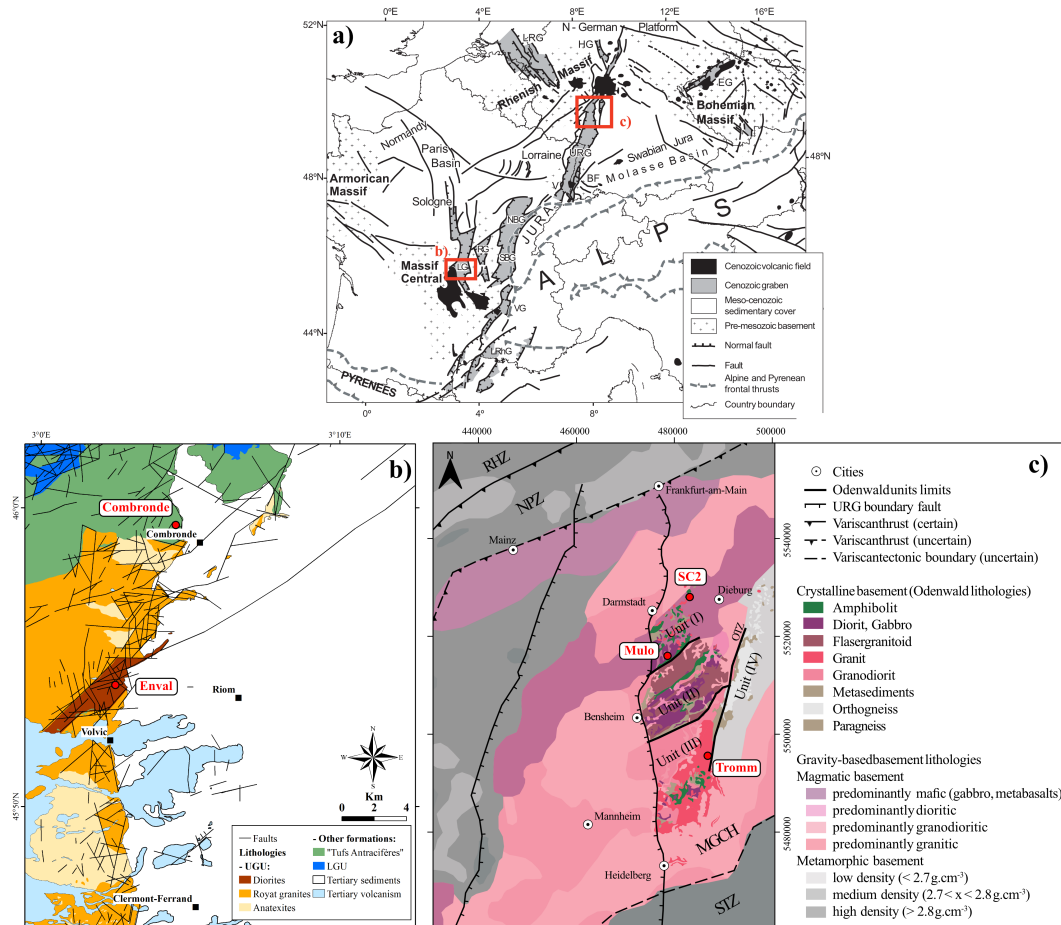


Figure 1. a) Map of the West European Rift System (WERS) and main tectono-sedimentary structures modified after Bourgeois et al. (2007) (URG & LRG: Upper & Lower Rhine Graben, NBG & SBG: Northern & Southern Bresse Graben, RG: Roanne Graben, VG: Valence Graben, LRhG: Lower Rhône Grabens, HG: Hessian Grabens, EG: Eger Graben V: Vosges and BF: Black Forest), b) Geological map of the outcropping basement at the shoulders of the Limagne Basin redrawn after Aubert et al. (1973); Barathon (1979); Bouillet et al. (1972); Dadet et al. (1980), Giot et al. (1986 carte aigueperse ref à trouver), Barbarin et al. (carte maringues à trouver en ref encore)(1988), with location of the studied outcrops : UGU & LGU : Upper & Lower Gneissic Units; c) Geological map adapted from Thews (1996) for crystalline basement lithologies from the Odenwald, and Frey et al. (2022a) for lithological and tectonic boundaries based on the interpretation of the joint inversion of gravity and magnetics. Gravity and magnetics boundaries were extracted from Frey et al. (2022a), copyright Elsevier (2021). Outcrops are marked and colour coded according to their main lithology. Domain labelling: RHZ: Rheno-Hercynian Zone, NPZ: Northern Phyllite Zone, MGCH: Mid-German Crystalline High, STZ: Saxo-thuringian Zone, OTZ: Oetzberg Fault system. Outcrops labelling: SC2: Mainzer Berg, MULO: Mühlthal, TROMM: Tromm outcrop.

Mühlthal (MULO) belongs to a local gabbroic intrusion composing the central unit of the crystalline Odenwald. This gabbro unit, oriented mainly NE–SW, exhibits fault zones with cataclasis, clay infill and pluri-metric densely fractured fault damage



zones with an NNW–SSE and NNE–SSW orientation. Finally the most northern outcrop here integrated is in the Tromm
90 granitic pluton (Bossennec et al., 2022; Frey et al., 2022b). The SC2 profile was acquired in the Mainzer Berg quarry, where the
granodiorite is characterized by an enhanced heterogeneity of fracture intensities around weathered fracture and fault corridors
(Bossennec et al., 2021, 2022). The sampling of the pointclouds is performed for these three outcrops with a terrestrial Laser
scanner device (RIEGL VG 400) equipped with a Nikon Camera for RGB acquisition (Bossennec et al., 2021). Raw LiDAR
datasets have been processed using RiSCAN PRO and **access** CloudCompare software.

95 2.2 RECO3D workflow

Rock outcrops are 3D geometry objects that are more naturally treated as surfaces rather than just point clouds (Pauly et al.,
2008). We propose a two-step surface-based approach that instead of working directly on the point clouds (Wang et al., 2016).
The detection operates on a surface reconstructed from the point cloud.

100 The outline of the method is as follows:

- cleaning
- surface reconstruction
- fracture recognition
- 105 – filtering
- fracture properties extraction

2.2.1 Point cloud cleaning

After merging the LiDAR scans acquired on the outcrop, the 3D point clouds were inspected and manually cleaned. This first
step is needed to allow a proper surface reconstruction with the RECO3D tool by selecting only parts of the cloud where
110 fractures can be identified (Figure 2). It removes parts of the point cloud where the outcrop surface is eroded, and the fractures
are not clearly visible. With the terrestrial LiDAR, there are also parts where the point resolution is low due to the large angle
between the outcrop and the laser scanning during the acquisition, mainly the outcrop boundaries and the uppermost areas.
Particular attention is given to crop out small clusters of vegetations frequently found on outcrop surfaces in order to avoid
noises to the surface reconstruction algorithm (black arrows, figure 2).

115 2.2.2 Surface reconstruction and fracture planes recognition

Reconstructing the surface from an outcrop point cloud is challenging by itself. The algorithm must be robust given that data
quality issues can occur such as noises, under-sampled areas, vegetations, weathering etc. It also needs to be scalable as the

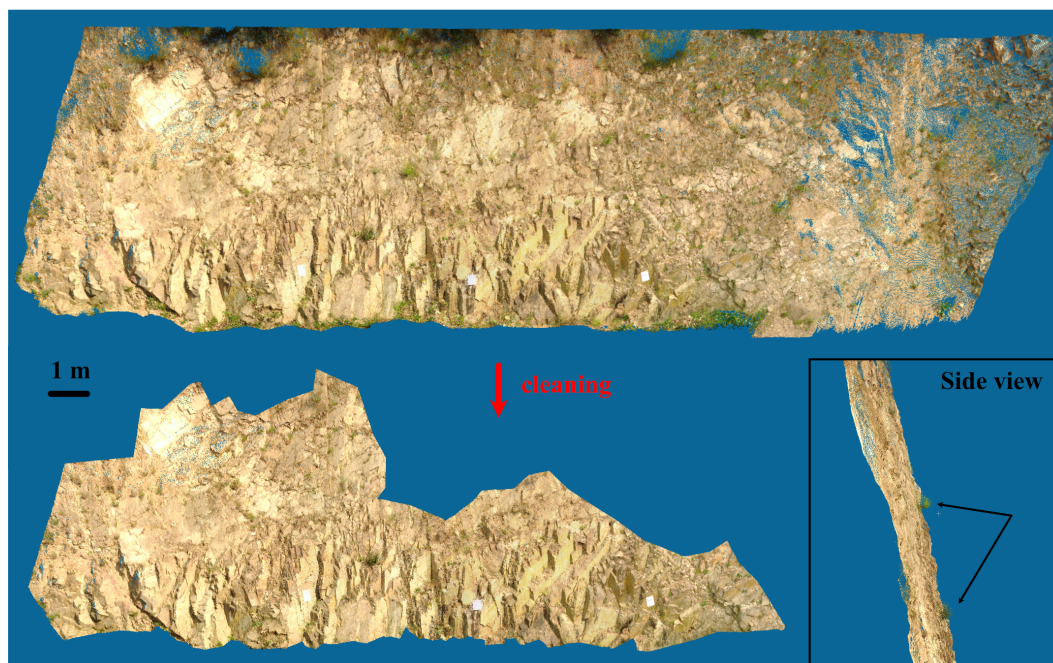


Figure 2. Example before and after cleaning step for Combronde point cloud with side view showing small clumps of vegetation that are removed for the further steps (black arrows).

point clouds get higher in **numerical resolution** or larger in physical dimensions.

In this work, we adopted an interpolating surface reconstruction method Simple and Scalable Surface Reconstruction (SSSR) to obtain the surface representation (Boltcheva and Lévy, 2016). The algorithm is resilient to aforementioned input point cloud quality issues. In terms of speed, SSSR is an order of magnitude faster than Poisson reconstruction and is highly parallelizable (Hoppe, 2008). At the end of the process, a triangulated surface having vertices collocated with the point cloud is produced.

For the automatic fracture recognition phase, **we propose a region-growing segmentation** approach based on information of the points computed easily from the reconstructed triangulated surface. For each of the non-boundary vertices on the surface, a plane is fitted to its one-ring including itself in a least-square fashion. A fitting error to the fitted plane of each vertex is computed. Certain vertices are selected as seeds based on their small fitting error to their respective plane.

Then, to grow a fracture from a seed, the **vertices in its topological neighbourhood** are evaluated in a ring-by-ring manner. A vertex is added to the current fracture when the following three user-defined geometrical criteria are satisfied:

130

- the vertex point distance to the current fracture plane $< \alpha$
- the standard deviation of the distance of the all the vertex points including the new one to the current fracture $< \beta$



- the angle between vertex normal and fracture plane normal $< \gamma$

The current fitted fracture plane is updated whenever a new vertex is added. The region-growing process stops when no new
135 vertex is added in the last vertices ring.

Such region-growing method is efficient by taking advantage of the geometrical and topological information provided by the reconstructed triangulated surface. Having only three parameters offers the simplicity of execution whilst sufficient flexibility to process point clouds of different data qualities and rock types through adapting different parameter settings.

140 2.2.3 Fracture filtering

When the best-fit parameters are found for the fracture recognition on the 3D point cloud, a last step of filtering is necessary to extract individual fracture plane from other parts of the outcrop. For the five studied outcrops, a first filter (filter I) is applied by removing planes with lengths inferior to the resolution of the smallest fracture visually identified (Figure 3). It excludes small irregularities and areas of lesser quality on the point cloud. The cut-off length used during filtering depends on the outcrop
145 quality and is discussed in the result section. Two other filters are tested and compared in this study. On filter II, features which are not identified as fracture planes are removed manually. Finally, filter III is an automatic filter of the fracture length that best fits to the manual picking (filter II) by moving the length cut-offs. The later was not performed on the MULO outcrop because no satisfying length parameters could be found due to the quality of the 3D point cloud (see 3.1 section).

2.2.4 P10, P21 and P32 computation

150 Fracture properties that are automatically computed are: orientation (strike, dip and dip azimuth), length with L_{max} = the maximal length of the fracture plane and L_{min} the minimal one, area and X, Y, Z coordinates of the fracture centre. For comparison between classical 1D scan lines data or 2D fracture maps, fracture intensity is also computed on the filtered results. The fracture P10 (fracture intensity = number of fracture/length unit) is obtained by drawing a virtual scan line on the point cloud and extracting of the fracture planes that crosscut the line. To estimate P21 (intensity = length of fracture/area unit of the
155 outcrop surface), a very smoothed surface fit is computed from the data point cloud. The result is a flat surface decomposed in cells of the variable surface. Let $\vec{U}_{i,1}$ and $\vec{U}_{i,2}$ be the two vectors starting from the same vertex and defined by the adjacent edge of a cell i , and $\vec{U}_{i,3}$ and $\vec{U}_{i,4}$ the vector starting from the opposing vertex and defined by the two other edges. The area S_1 of the cell can then be obtained using equation 1.

$$160 \quad S_1 = \frac{|\vec{U}_{i,1} \times \vec{U}_{i,2}| + |\vec{U}_{i,3} \times \vec{U}_{i,4}|}{2} \quad (1)$$

The total area S is then calculated by adding the area of each cell using equation 2, where n is the number of cells.

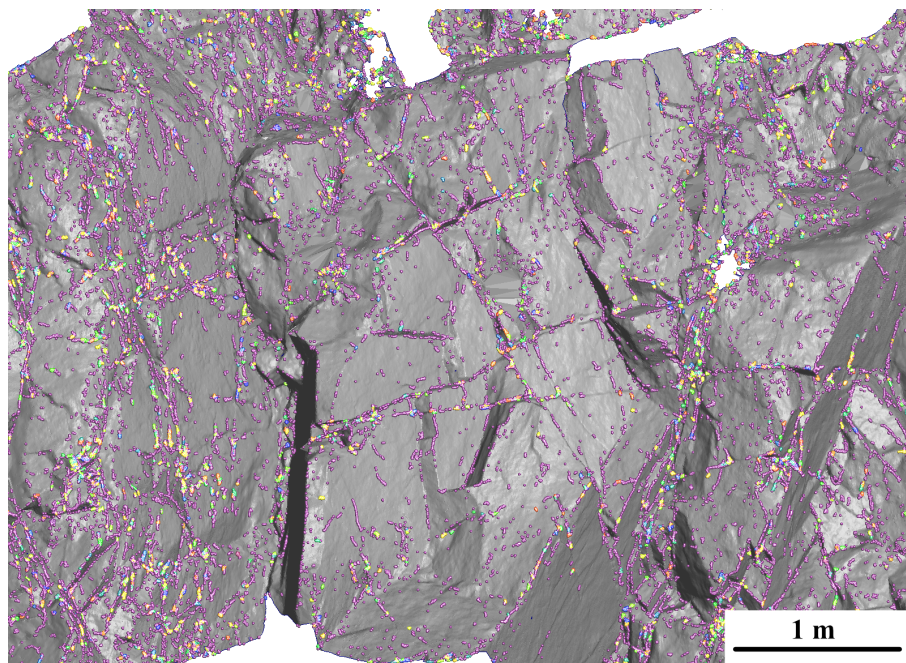


Figure 3. Small irregularities filtered by filter I on the Enval point cloud.

$$S = \sum_{i=1}^n S_i \quad (2)$$

Then P21 is easily obtained by dividing the total number of fractures by the obtained surface.

To estimate P32 (fractures area/rock volume unit), a surface fit is computed from the data point cloud, without a smoothing factor. The result is a surface with a tight fit of the surface of the outcrop. The volume V between the smooth and tight fit surface is then computed using the integral of the absolute differences between the surfaces. The integration is approximated using the trapezoidal rule twice (in x and y directions), i.e. for x:

$$\int f(x)dx \approx \frac{1}{2} \sum_{i=1}^n (f(x_{i-1}) + f(x_i))\Delta x_i \quad (3)$$

where n is the number of cells in the integration direction (x or y), and $\Delta x_i = x_i - x_{i-1}$. Then P32 is easily obtained by dividing the total fracture area by the obtained volume. Figure 4 illustrates the procedure.

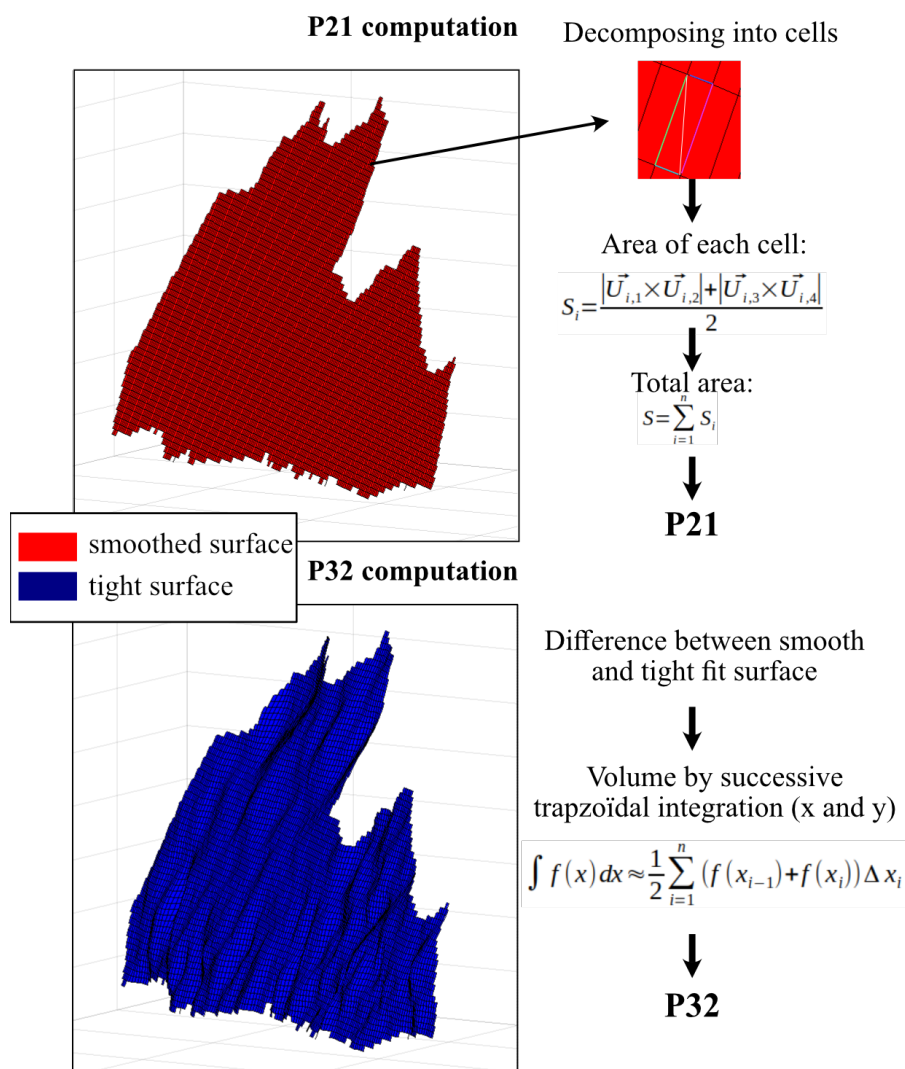


Figure 4. Illustration of the P21 and P32 computation procedure. Combronde outcrop.

3 Results

3.1 3D Mesh comparison

In the first step, the 3D point clouds acquired on the outcrops are cleaned following the methodology described in section 2.2.1. The resulting point clouds vary between 0.8 M to 4.67 M points for outcrop lengths from 18 to 52 m.

175 They are qualitatively classified after visual inspection of the point cloud and the generated tetrahedral surface (Figure 5). The point cloud from Enval (3.15 M points) is the most promising, because it contains very few vegetation areas and associated holes

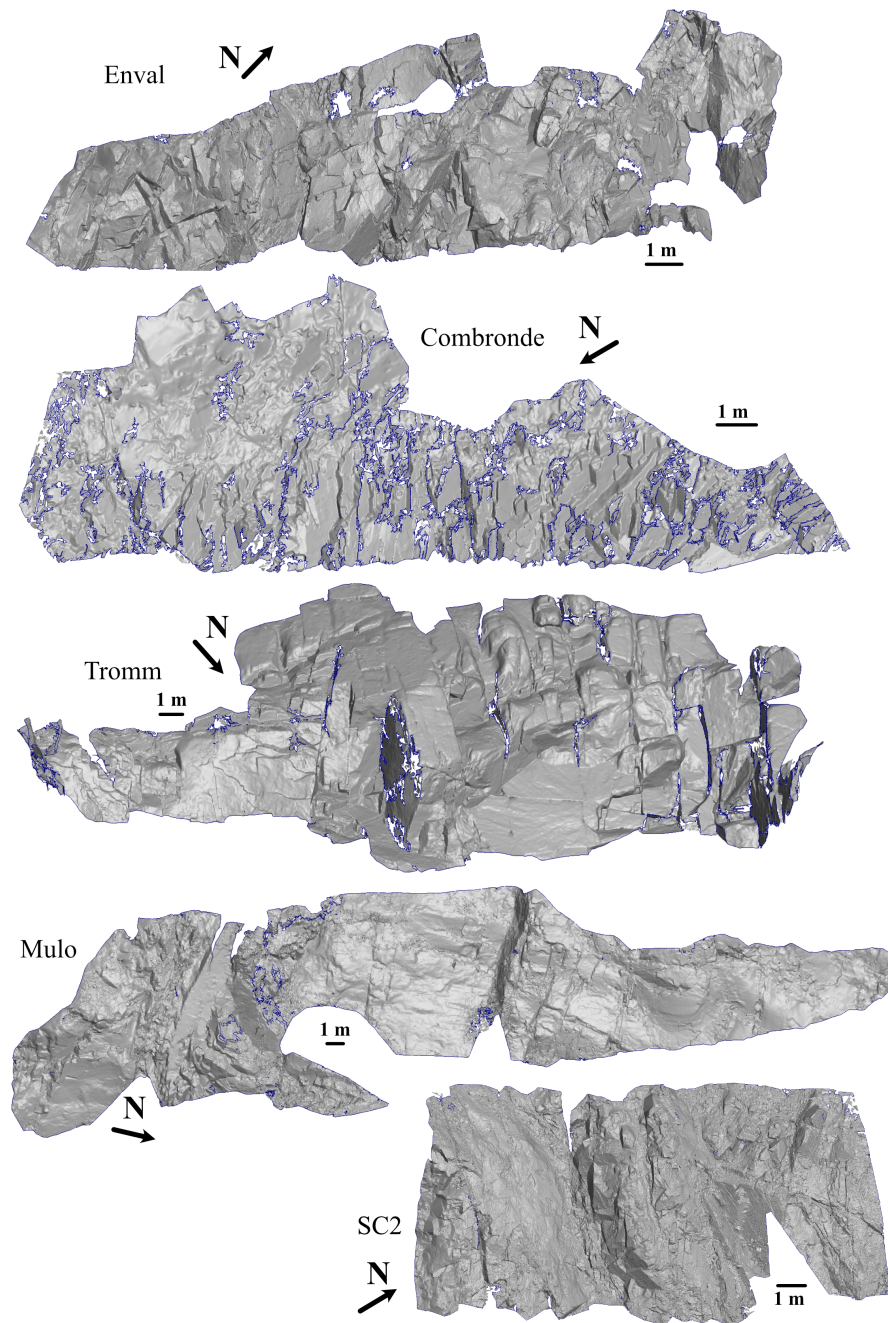


Figure 5. View of the outcrop surfaces reconstructed from the 3D point cloud after cleaning.

or blurry surfaces after its reconstruction. Many fractures have a significant outcropping surface and they seem homogenously distributed on the outcrop. The point cloud from Combronde (4.67 M points) also displays good quality at the bottom, but there



Table 1. RECO3D parameters tested on each point cloud.

Parameters	Test A	Test B	Test C	Test D
Vertex point distance (α)	0.08	0.06	0.04	0.02
Stdev total vertex distance (β)	0.05	0.04	0.03	0.01
Vertex vs fracture plane normal angle (γ)	0.08	0.06	0.04	0.02

is a blurry area above 2m height. In details, the LiDAR data have a lesser quality for fractures with surfaces with a high angle from the acquisition point. The point cloud from Tromm (2.00 M points) is equivalent to Combronde in terms of vegetation and fractures offsets, but many of them are partly weathered and eroded. They have thus a convex shape, not strictly planar, which is assumed to be a difficulty for the developed tool. MULO (3.15 M points) and SC2 (0.80 M points) are the two poor-quality outcrops, with a large part of eroded surface and large parts with vegetation that induce a smoothed tetrahedral surface.

3.2 Fracture plane recognition with different parameters

Several parameters have been tested on each point cloud, from large α, β & γ variations to more restricted ones (Table 1). The results of the different tests are presented for the Enval outcrop in Figure 6 to compare an area with sharp fracture offsets (1) and another with higher fracture rugosity and/or more eroded surface (2). For type (1), the plane recognition is efficient for most of the fractures with the largest parameters, i.e. during Test A. Test B and C show quite similar results in a first order view (blue in figure 6). In details, some fractures with similar orientation and a common edge may be grouped in a unique plane with a mean orientation (black circles in figure 6), Test C offers then the bests results. For Test D, the set parameters become too restrictive, and many fractures are subdivided into several planes, indicating that the fracture recognition reaches to its limit. These observations are similar for outcrop type (2), but it becomes critical, especially for large fracture planes which are eroded and with some rugosity, or when several fracture planes with a similar orientation are close to each other (purple circles in figure 6). For these, Test A and B tend to merge several fractures in a big plane with a mean orientation. On the contrary, Test D is too sharp and decomposes these areas too much and introduces unwanted noise.

These observations were similar for the five tested point clouds. It is thus possible to conclude that in the first order, the RECO3D tool seems efficient for an automated fracture plane recognition, with the best fit with Test C parameters. Indeed, its parameters are the best compromise between the noise on the small fracture planes and in rugous areas of the outcrop, and the over-averring of the big fractures' planes, which are not desired. Moreover, a manual check is possible to merge the rugous fractures-planes divided into several planes by the automatic reconstruction in a second step. For these reasons, the results on the other outcrops are presented with Test C parameters in the following sections.

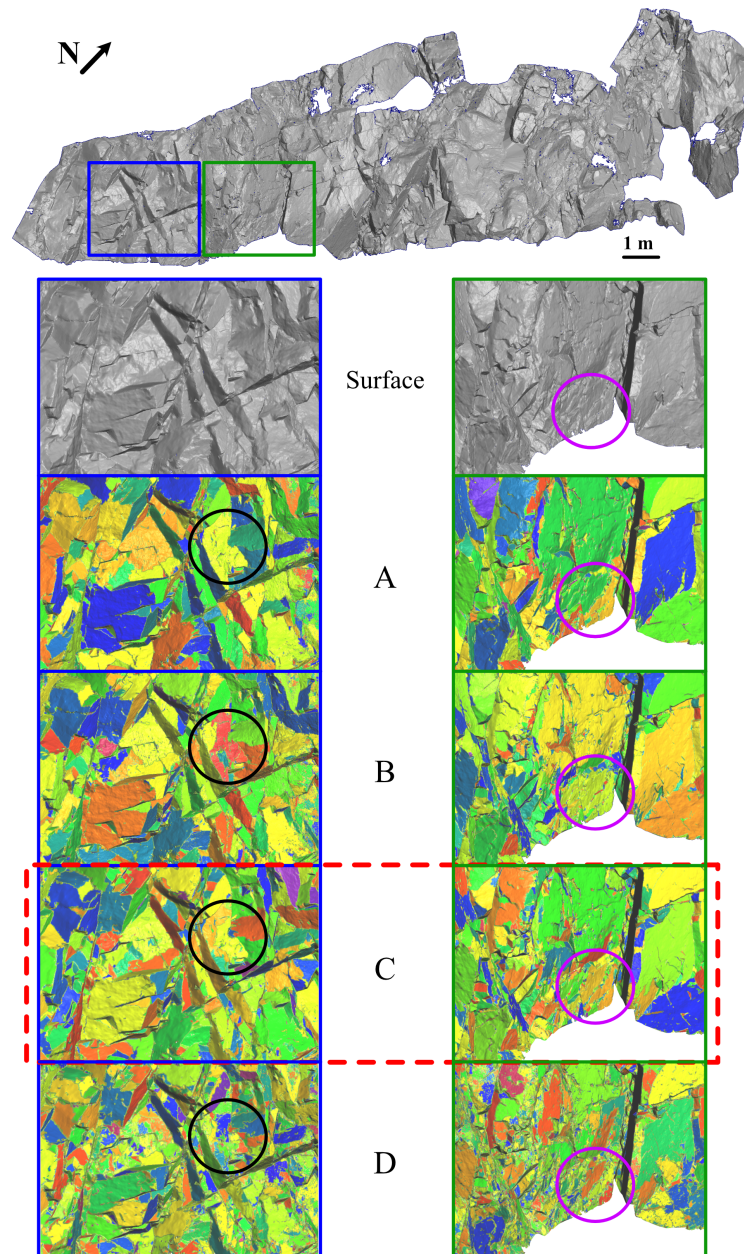


Figure 6. Visual comparison of the different parameters for RECO3D tool on Enval outcrop in an area (1) with sharp fractures offsets (blue) and (2) with an eroded surface (green). Each coloured patch is a reconstruction fracture.

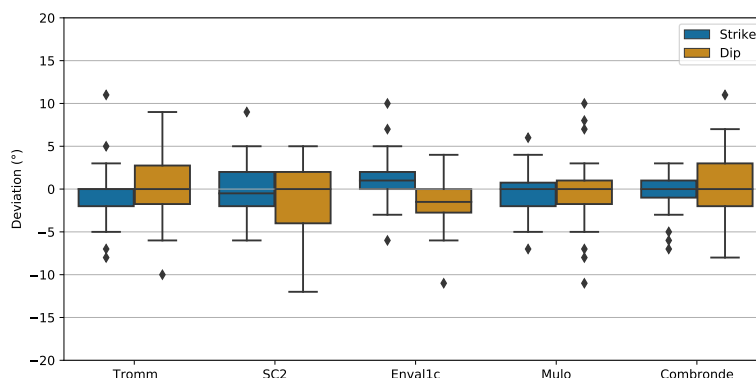


Figure 7. Difference between manual plane picking tool Compass 2.0 of CloudCompare® and RECO3D fracture orientation data on 30 random planes for each point cloud, presented in box plots for Dip and Strike.

3.3 Quality check of the automatised recognition

205 To quantitatively test the quality of the fracture reconstruction, the orientation of 30 fractures planes randomly picked on each outcrop is compared between Test C results and the fracture orientation picking tool of CloudCompare® software (Compass 2.0) (Figure 7). This tool allows to pick points from the cloud in a given circular area and estimates the orientation of a plane fitting all points using least squares regression (Thiele et al., 2017). The comparison shows that most planes are in a range of -3 to +3 degree in dip azimuth and dip. The few planes with a more significant difference are small planes where few points could
 210 be picked with the circular tool, or with a small point density linked to the LiDAR acquisition process, or at the contrary large planes with a certain curvature. For the latter, the orientation given by the pinking tool clearly depends on the picked position while the RECO3D tool calculates the mean orientation of the whole fracture. The observed differences are thus globally consistent given the different calculation methodologies between the two tools. Moreover, for a natural fracture, the variation in dip and dip azimuth linked to fracture roughness and curvature is also commonly in a 10° range when measured in the field,
 215 with a compass for instance. Thus, the fracture orientation calculated after the fracture reconstruction with our RECO3D fits well with data acquired in the field.

3.4 Data filtering and fracture parameters

For the five outcrops filters I, II and III are applied on the fracture plane construction with parameters from Test C. Filtered fracture lengths are shown in table 2. The results in orientation and length distribution are discussed for each outcrop below.



Table 2. Minimal and maximal fracture length filtered automatically by filter I and III on the five digital outcrops and the number of selected fracture plans on each filter I, II and III.

Outcrop	Filter I			Filter II	Filter III		
	Lmin (m)	Lmax (m)	Fractures	Fractures	Lmin (m)	Lmax (m)	Fractures
Enval	0.01	3.5	13098	9698	0.1	3.5	1591
Combronde	0.035	3.5	2577	1411	0.14	3.5	768
Tromm	0.06	8	3197	2058	0.34	8	565
MULO	0.04	10	2318	1563	x	x	x
SC2	0.09	4.5	1796	901	0.3	4.5	471

220 3.4.1 Enval

On Enval outcrop, the plane reconstruction with the filter I parameters contains 13 098 fractures with lengths between 0.01 and 3.5 m (Appendix A). Visually, the fracture network is very well represented in the parts of the outcrop where the fractures are clearly identified. Only few areas of noise remain where the surface is degraded despite cleaning the point cloud. The fracture orientation diagrams in number show a very heterogeneous fracture network, around the main fracture directions distributed mainly from N000°E to N055°E (Figure 8). The length weighting on the orientation partly solves the problem, and distinct fracture sets can be distinguished at around N050°E and N175°E. The length distribution shows two power law trends for fractures shorter and longer than 0.8 meters respectively. Filter II, which is the manual removing of planes that are not fractures, decreases the planes number to 9 698, but the orientation and length distribution remain similar to filter I. With filter III, the main fractures orientations N050°E and N175°E are visible on both orientation diagrams, in number and length, with secondary fracture sets that can be pointed around N005°E and 110°E (Figure 8). The length distributions are consistent between the three types of filters, with a two-step power-law exponent.

3.4.2 Combronde

The minimal fracture length for the filter I on the Combronde outcrop is slightly higher than for Enval, with 0.035 m instead of 0.01 m, for 2 577 reconstructed planes (Table 2). The outcrop view shows the fracture plane reconstruction excludes a large part of the top where fractures are not clearly defined (Appendix B). The orientation distribution highlights that the fractures are concentrated in dip between 30 and 90° and dip direction between N090°E and N180°E (Figure 9). Three fracture sets can be identified on the rose diagram, especially after applying the length weighting, with main strike N005°E, N030°E and N070°E. The lengths have a clearly defined power law distribution with an exponent of -2.1. The manual filtering reduces the total fracture number to 1 412. They are mainly removed on the border of the model and in the noise of the top of the outcrop. On this one, the three main sets are the same as filter I, with only a slight shift of orientation for fracture set 2, from N030°E to N040°E, and a reduced fracture intensity compared to the N005°E set. Finally, the result on filter III with an automatic length

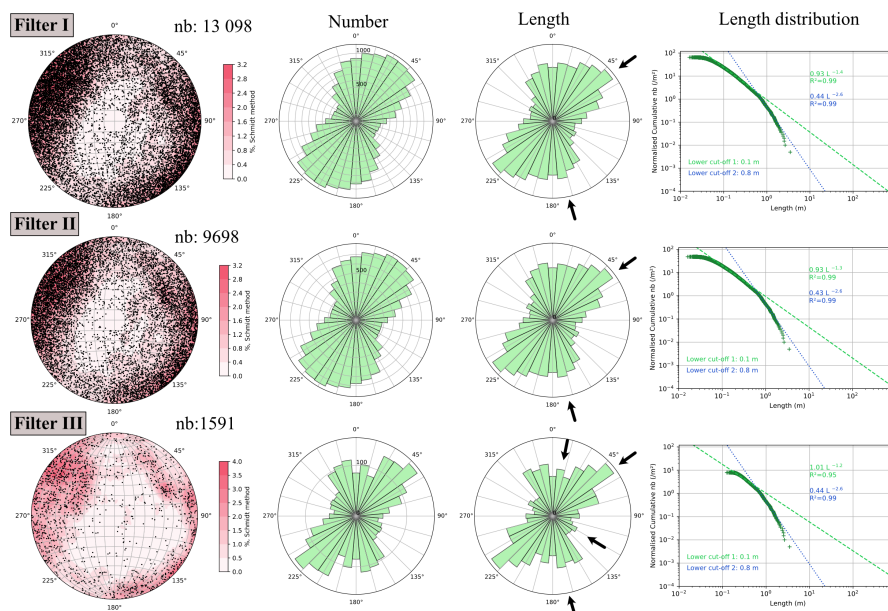


Figure 8. Stereographic view of the fracture plane poles, orientation rose diagram in fracture number and length weighted and length distribution plot on the three filters applied to Enval fracture reconstruction.

filtering, with a lower cut-off at 0.14 m instead of 0.035 m, are quite similar. Only the proportion between the three fracture sets varies. The length distribution on the three filters also remains quite similar.

3.4.3 Tromm

245 The first step of filtering on the Tromm digital outcrop includes the planes reconstructed with lengths between 0.06 and 8 m, which are larger than Combronde and Enval outcrops, with a total of 3 197 planes (Table 2). Indeed, the Tromm outcrop exposes mostly large fracture planes after visual inspection. Such results are thus expected (Appendix C). Orientation distributions show the main fracture set N150°E, with a cluster of dip around 45° to the SW, and two secondary fracture sets around N070°E and N120°E (Figure 10). Filter II decreases the validated fracture planes to 2 059. The cleaned areas are mostly on the horizontal surfaces of the outcrop, which are eroded and poorly constrained by the terrestrial LiDAR data (Appendix C). On this filter, 250 the main fracture sets remain identical to filter I, as the length distribution with a power law with an exponent around -1.8. It is also the case for filter III, an automatic filter of plane length between 0.35 and 8 m.

3.4.4 MULO

Filter I for MULO outcrop has a total number of reconstructed planes of 2 318 with lengths between 0.04 and 10 m (Table 2). 255 This outcrop difficulty is that there is large fractures and eroded surface combined with areas with high a density of short fractures (Appendix D). A part of the selected planes is clearly linked to noise on the outcrop surface but filtering longer

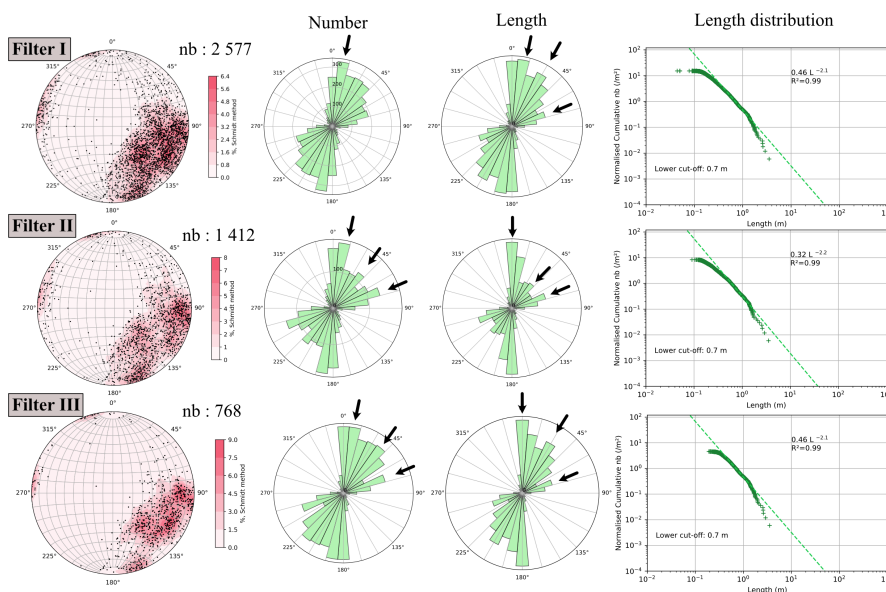


Figure 9. Stereographic view of the fracture plane poles, orientation rose diagram in fracture number and length weighted and length distribution plot on the three filters applied to Combronde fracture reconstruction.

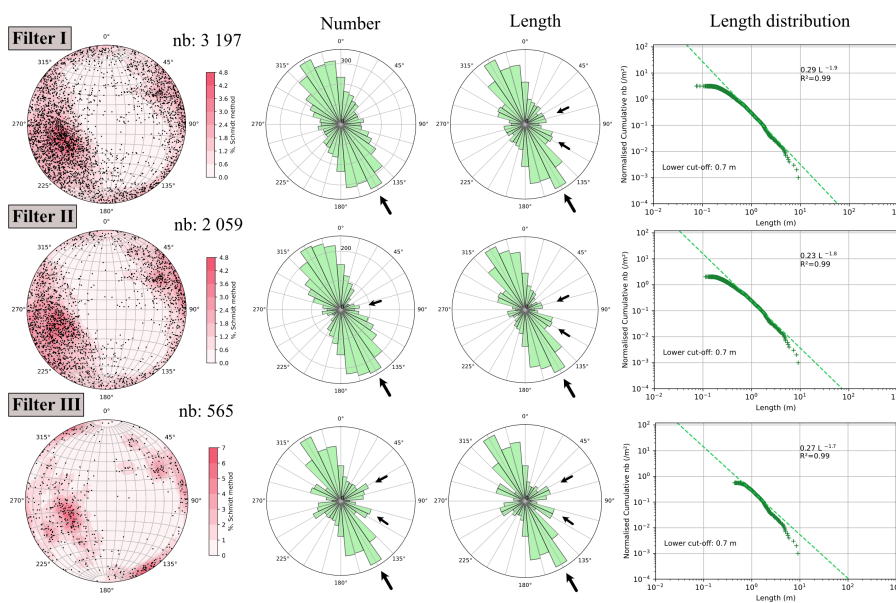


Figure 10. Stereographic view of the fracture plane poles, orientation rose diagram in fracture number and length weighted and length distribution plot on the three filters applied to Tromm fracture reconstruction.

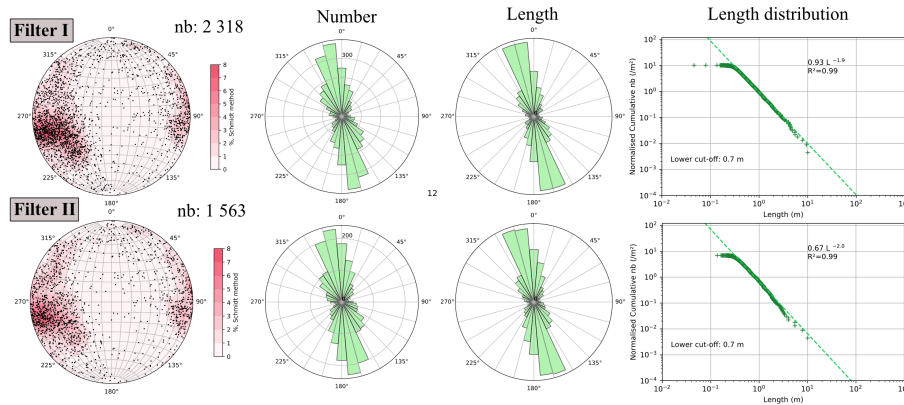


Figure 11. Stereographic view of the fracture plane poles, orientation rose diagram in fracture number and length weighted and length distribution plot on filters I and II applied to MULO fracture reconstruction.

planes also implies deleting fracture planes clearly observable on the digital surface. It is why filter III was not applied here. The manual filtering reduces the number of planes to 1 563, mostly by removing further the surfaces with noise linked to erosion and small vegetation that could not be removed in the point cloud cleaning phase (Appendix D). The orientation rose diagram on the two filters shows similar results, with the main fracture set with a N170°E strike and dip mostly > 60° to the W (Figure 11). The length distributions of the two filters are quite similar, with a lower cut-off at 0.7 m and a nice fit.

3.4.5 SC2

The first step of filtering (filter I) for SC2 outcrop with 1 796 validated planes shows two large areas where the outcrop surface is too smooth due to erosion for the fracture network modelling (Appendix E). Out of these two areas, the fracture network can be divided into three main fracture sets N010°E, N030°E and N050°E (Figure 12). A minor set N160°E should also be identified after weighting by the lengths. These results are similar to the manual filtering (filter II) for the three main sets. Only an additional minor set with N090°E orientation appears. The filter III selection decreases the estimated fracture number to 471. Most noised planes are removed, but the sharp filtering of the planes with length < 0.3 m also deletes a part of the fracture planes that we can recognize by visual inspection. It has for consequences to minimize the fracture sets N010°E and N150°E mostly (Figure 12). In contrast the power law fit remains almost constant between the three filters because the filtered planes on filters II and III are out of the power law fit thresholds.

3.4.6 General comparison of the results

RECO3D has been tested on five outcrops of basement rocks with different exposure qualities and varied fracture networks. The calibration step for α , β & γ parameters used for the automatic fracture planes reconstruction show that the tool can detect a large part of the fracture network. The parameters are mostly used to refine the detection for parts of the point cloud where the fractures are not clearly defined, either because of the outcrop quality, or the fracture network itself (high density of small

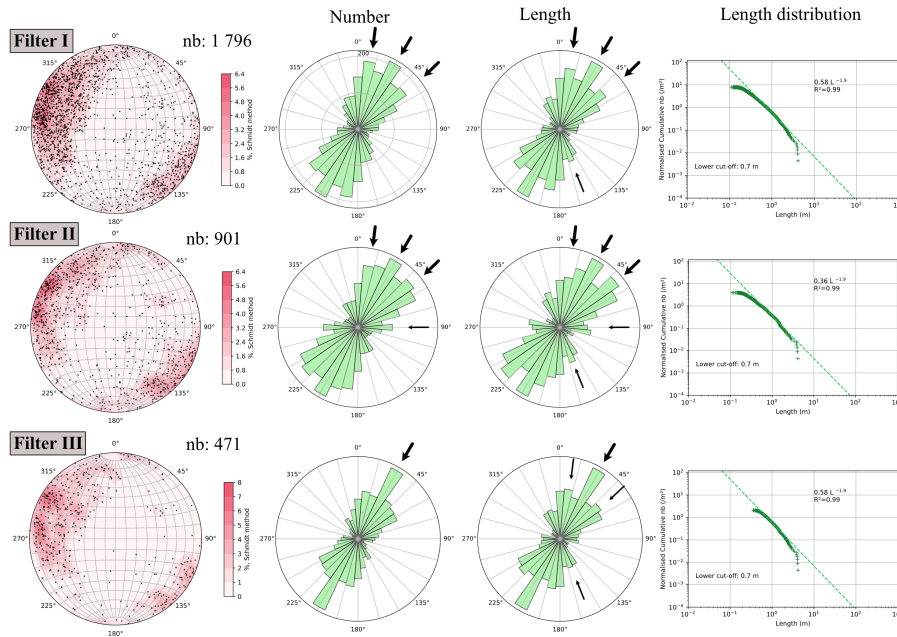


Figure 12. Stereographic view of the fracture plane poles, orientation rose diagram in fracture number and length weighted and length distribution plot on filters I and II applied to MULO fracture reconstruction.

planes, low angle between ~~to~~ fractures, ~~---~~). After the calibration step, automatic filters and time-consuming manual filtering have been performed to separate the fracture planes from the planes linked to noise and part of the outcrop surface that were not fractures. The manual filtering results (filter II) can be considered as the reference, meaning that it is the equivalent of a manual drawing of the fracture planes on the point cloud. Filter I is a “smooth” automatic filtering, as it removes the small planes linked to the reconstruction process, and filter III is “sharper” and also deletes a part of the fracture data in case where the outcrop quality is reduced (for MULO & SC2 in this study tests). On the five outcrops studied, not matter of the outcrop quality, the smooth filter shows very similar results to the manual picking results in terms of orientation distribution (length weighted or not) and lengths distribution. Moreover, this is if the fracture network is composed of a single fracture set like MULO outcrop or with a more complex network like in Combronde or Enval. The sharp filter is also consistent with ~~the~~ manual filtering, ~~even~~ if the filtering process deletes some fractures. The largest differences are observed for SC2 and Enval outcrops. For Enval (the best quality), the sharp filtering allows detecting two fracture sets that are drowned in the noise around the primary fracture set orientation even in the manual filter data (Figure 10). However, there is also a cut-off with two power laws for the length distribution that indicates a change in the fracture network properties between the fractures longer than 0.8 m and the shorter ones. The change in the orientation distribution between filter I and III suggests thus more likely a natural change in the fracture pattern, with different fracture sets between the two scales, than a problem in the fracture plane reconstruction. For SC2, between filters I and III, there is mostly a loss of intensity of two main fracture sets (N010°E and N050°E) and a minor one (N090°E). On this outcrop, we have shown that due to the bad quality of the point cloud, the sharp removal of noised planes



also removes ~~a large part of~~ fracture planes.

295

In conclusion, as long as the outcrop and associated point cloud are of **sufficient quality**, we are confident that the RECO3D tool is efficient in detecting the natural fracture sets and the associated fracture properties. Both manual and automatic filtering show significantly the same results, which allows the geologist to consider the time saving for fracture characterization if the manual inspection is not needed or reduced to a global visual check of the results. However, filtering by the length to separate planes linked to noise and fractures remains limited, and further developments must be made to enhance the automatic filtering process, for example, combining other parameters in the filter. Removing areas linked to the natural erosion on the outcrop surface also remains ~~a challenge~~. It will be of particular interest for sedimentary layered rocks, for which the outcrop geomorphology is more commonly built by rock erosion compared to basement rock outcrops. For those, introducing outcrop rugosity criteria to reconstruct the fracture planes only will be an important step of development.

300

305 4 Discussion

RECO3D has been developed to enhance productivity and statistic robustness of fracture network analysis workflow. The plugin encompasses automated processes, data analysis, and visualization, offering comprehensive support for elevating one's work. It also allows statistical analysis in 3D and comparison with 2D and 1D field mapping, and proposes an accurate quantification of fracture network properties for further integration into fractured reservoir flow and finite elements models.

310 4.1 3D plane reconstruction vs classic data

As the outcrop is usually exposing one wall, uncertainties remain on the 3D mapping of the structures. The outcrop is representing a ~~kind of slice in~~ the 3D rock mass, and the fracture surface detected by the tool is only the exposed part of the whole fracture. Indeed, the acquired data depends on the fracture orientation versus the mean orientation of the outcrop and the exposure condition. Ideally, if several walls orientations are available at one location, they should be all integrated in the fracture network ~~features~~ quantification.

315

4.1.1 Comparison with 1D scan lines

To explore the representativeness of this new type of data, we performed classical scan lines (SL) on Enval and Combronde outcrops. For each, a virtual SL on **filter II** has been drawn on the RECO3D plane reconstruction to extract the fractures planes data at the same position as the field SL (Appendices A & B).

320

As we have seen on Enval outcrop, there is a threshold in the fracture network with two different properties around the 0.8 m fracture length (Figure 8). On the outcrop data, this threshold is also evident (Figure 13). Thus, the fractures' orientation are compared regarding this threshold. For the fractures longer than 0.8 m, the virtual SL shows very few fractures (24 vs 71 in the field) which makes the orientation statistics ~~not~~ interpretable. For the fractures shorter than 0.8 m, the sampled number is quite

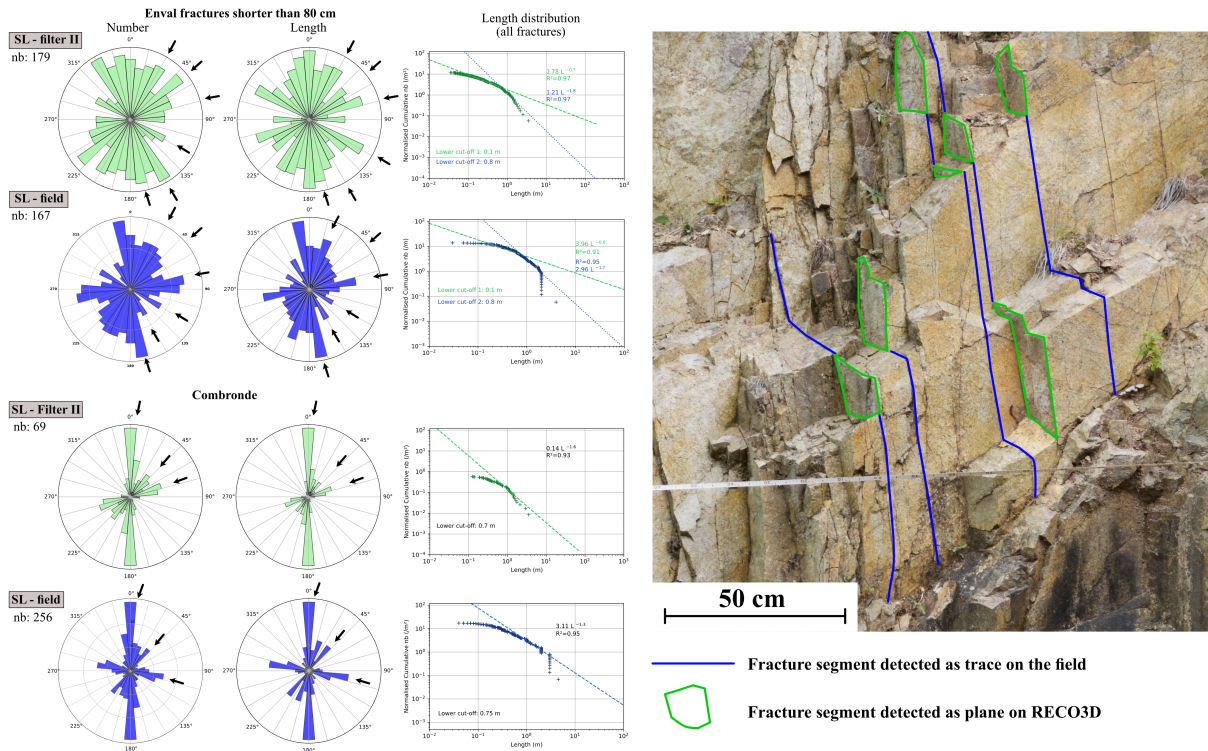


Figure 13. 1D scan lines comparison on Enval and Combronde outcrop, between the fracture planes detected by RECO3D (green) and the classic sampling methodology in the field (blue).

325 similar (167 on the field and 179 for RECO3D). As observed on the whole outcrop with the RECO3D detection (Figure 7), the fracture network is scattered even for the field data with at least 6 fracture sets (N030°E, N045°E, N075°E, N120°E, N150°E and N170°E) (Figure 13). Even if the proportion of each set varies between the outcrop and the virtual SL, both dataset show the same kind of result.

330 The fractures extracted from the virtual SL for Combronde are far fewer than in the field, respectively 69 vs 256 (Figure 13). As for Enval, more longer fractures are sampled in the field than on the virtual SL. On both, the main fracture set is N000°E oriented as on the whole outcrop analysed by RECO3D (Figure 9). There is also a minor fracture set around N045°E direction, but the N100°E set on the outcrop is not represented on the virtual SL. At the opposite, a N065°E fracture set is on the field data but not in the RECO3D data.

335

Both comparisons between the field and virtual data show similarities but fits not perfectly. Two causes are identified and linked to the inherent difference between the two sampling methods. First, the RECO3D tool which works with the detection of fracture planes on the outcrop surface will not detect fractures that are only as fracture trace on the outcrop (picture example



in figure 13). In the case of Combronde, these fractures observed by the geologist in the field are mainly N100°E, direction that
340 RECO3D failed to detect. However, there is no reason for it to be systematically the same fracture set that suffers from this
sampling effect. Combronde thus seems to us to be a special case on this point. The second reason is the length of the fracture
sampled. Indeed, in the field the geologist correlates fractures traces and fractures surfaces which are with the same orientation
(~~picture~~ example in figure 13). Such fracture is at this stage divided in several planes with the RECO3D tool. This will led to
~~more short~~ fractures with small orientation variations against on single long fracture identified on the field. Even if the two
345 sampling methodologies will never be the same, these differences can be worked in a second step of development. Indeed, with
the spacial location of each fracture plane, it will be possible to merge adjacent fracture surfaces with he same orientation as
~~do the geologist in the field~~, and also add imagery detection technologies for the detection of fractures only visible as fracture
traces (i.e. ref).

4.1.2 Comparison with 2D maps

350 Length distributions of fracture traces mapped on fracture maps or on 1D scan lines show in some cases and exponential law
linked to mechanical layering, induced by strata boundaries or grain size, depending on the scale of the studied fractures (refs
odling etc). A power-law distribution is shown for fracture networks linked to tectonic activity, and fault zones, in non-layered
rocks as those studied here (refs). In the latter case, the power-law is defined in a length range with cut-offs lengths linked to the
355 sampling method, i.e. roughly the resolution of the map (censoring effect) for the shorter traces and the truncation of the traces
longer than the map size or outcrop size (truncation effect) (Bonnet et al., 2001). It is therefore shown that the law exponent is
dependent on the sampling dimension and the geological context. Thus, if scan line data will show an exponent $a \approx 1$, fracture
maps on the same geological object should show a length distribution with an exponent $a \approx 2$, and the fracture network
modelled in 3D and size distribution with a ≈ 3 . Concerning the five outcrops studied, the fracture network of Combronde
shows a length distribution with exponent of 2.1-2.2 depending on the filters, Tromm between 1.7 and 1.9, MULO between 1.9
360 and 2.0 and SC2 of 1.9. The value of Enval is partly due to the two-step power law.

Interestingly, the length of the planes reconstructed by the RECO3D tool shows distribution similar to the classic fracture traces
maps, with an exponent of around 2. It means that the length distribution from the RECO3D tool may be used in the same
way as the classic 2D methodology and extrapolate in the same way for input in numerical fracture network models such as
DFNs. As the proposed automatic reconstruction can be performed in a few hours compared to fracture manual digitalisation
365 that are much more time-consuming, it promises a great gain of performance for such structural analysis. In addition, the tool
provides the fracture area for the first time, which completes the geometric characterization classically only tested with the
fracture lengths. This new kind of data will be studied in the next step to integrate them into the fracture modelling workflows.

4.2 Further implementations for DFN models

One of the most challenging parts of the conversion between field data and fracture network modelling is the calculation of
370 the fracture network density. Once the fracture sets and geometrical properties are defined, the fracture intensity P10 (fracture
intensity = number of fracture / length unit) obtained on 1D SL or P20 (density = number of fracture / area unit) and P21



Table 3. Table of calculated area, volume and associated P21 and P32 intensity for each filter applied on the five studied outcrops.

Outcrop	Area (m^2)	Volume (m^3)	Filter I		Filter II		Filter III	
			P21 (m^{-1})	P32 (m^{-1})	P21 (m^{-1})	P32 (m^{-1})	P21 (m^{-1})	P32 (m^{-1})
Enval	110	30	119.1	4.1	88.2	3.7	14.5	3.3
Combronde	100	6	25.8	13.5	14.1	8.6	7.7	10.6
Tromm	310	210	10.3	1.9	6.6	1.5	1.8	1.5
MULO	420	125	5.5	2.5	3.7	1.6	x	x
SC2	140	50	12.8	2.7	6.4	1.6	3.4	2.1

(intensity = length of fracture / area unit) obtained on 2D fracture maps have to be converted for a 3D fractured rock mass, classically with P32 (fracture area / volume unit) (Dershowitz, 1984). Some general conversion tables exist (for example Wang (2005)) but the variability of the geological objects prevents the use of systematic corrections in many cases. In most studies, the conversion to P32 is evaluated by try and error method and calibrated with expected permeability or flow data (La Pointe et al., 2005; Niven and Deutsch, 2010). With its 3D data, the RECO3D reconstruction offers the opportunity to calculate P32 directly in a slice of the rock mass. After computing the outcrop area and volume following the methodology described in section 2.2.4., P21 intensity and P32 density are calculated for the three filters for each outcrop (Table 3). The computed volume is very low for Combronde because the outcrop is nearly flat except for the roughness related to the fracture network. On the contrary, MULO and Tromm show large volumes because of the few large fracture surfaces that segments the outcropping surface in different directions. Consequently, Combronde shows P32 density much larger than the other outcrops, as it is the second in P21 intensity, and MULO and Tromm show the lowest P32. The P32 depending on the filter varies from 1.5 - 1.9 m^{-1} for Tromm to 10.6 – 13.5 m^{-1} for Combronde. The comparison to published data is not simple because intensity values are linked to the lowest fracture length set, which is different for each study. Also, as mentioned before, most published P32 values are derived from P10 or P21 conversion and not direct data. For example, Miernik (2020) computed P32 from P10 on an outcrop in sandstones with values between 1.7 and 2.5 m^{-1} in damaged zones and 4.4 to 10.3 m^{-1} in fault cores; Bonnet et al. (2001) computed P32 in carbonates between 1 and 3.5 m^{-1} with the same methodology on P21, as Seers and Hodgetts (2016) on shear bands show P32 between 3.76 and 35.56 m^{-1} . At least, for these studies of fracture networks at almost equivalent scales, it shows that the computed fractures areas and volume by the RECO3D tool fits with the ranges obtained by P10 and P21 to P32 conversion. Therefore, the methodology to directly compute P32 from the outcrop volume which is a slice of the real 3D rock mass seems to be valid. It is a first step to directly compute DFN network from these new type of data in the future and reduce the uncertainties for this kind of models (Dashti et al., 2023; van der Vaart et al., 2021).



5 Conclusions

The new tool RECO3D presented here aims to reconstruct fracture planes automatically on 3D outcrop data, obtained using
395 LiDAR or photogrammetric acquisitions. This paper showcases the results from five outcrops of basement rocks with different
fracture networks and outcrop qualities. For this first step of development, we use three geometric parameters to detect planes
on a reconstructed surface from a point cloud, filter the fractures planes and extract their properties: orientation, length, area and
X, Y, Z position of the centre. The different outcrops tested shows that the tool is efficient for fracture planes recognition. The
geometric parameters fine-tuning is only needed to improve the results in noisy parts of the outcrop (due to outcrop erosion or
400 point cloud quality). Even if the filtering step may be improved, the comparison between manually extracted and automatically
filtered fracture planes shows similar results in orientation and length distribution. Thus, we consider our methodology fully
suitable for fracture network characterizations even if further developments will improve the automatic workflow, especially
for use on sedimentary rock outcrops. Sampling the fracture network is a critical step for geomechanical or flow modelling in
many contexts. Performing 1D sampling on the field or 2D fracture maps are particularly time-consuming and subject to well-
405 known sampling biases. The automatic fracture detection on 3D data offers the double advantages of catching many fracture
data in a short operating time and asses to the characterization of fracture networks in 3D. One of the most promising results
is additionally the direct calculation of P32 fracture intensity without using of proxies for derivation from 1D or 2D fracture
intensity data.

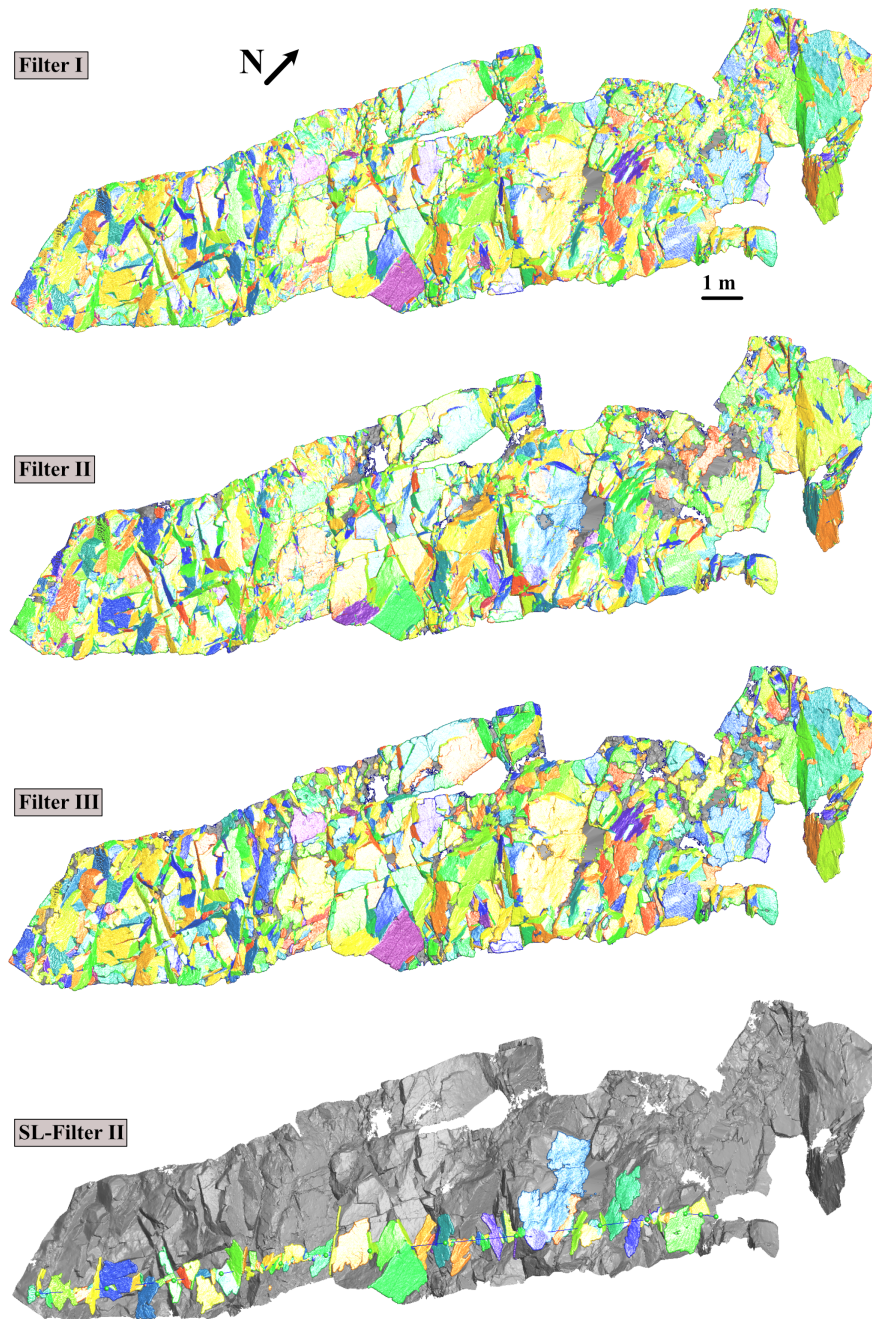


Figure A1. Picture of the fracture planes reconstruction (one colour = one fracture) from Enval point cloud with filter I, II and III and the digital scan line extraction from filter I and II.

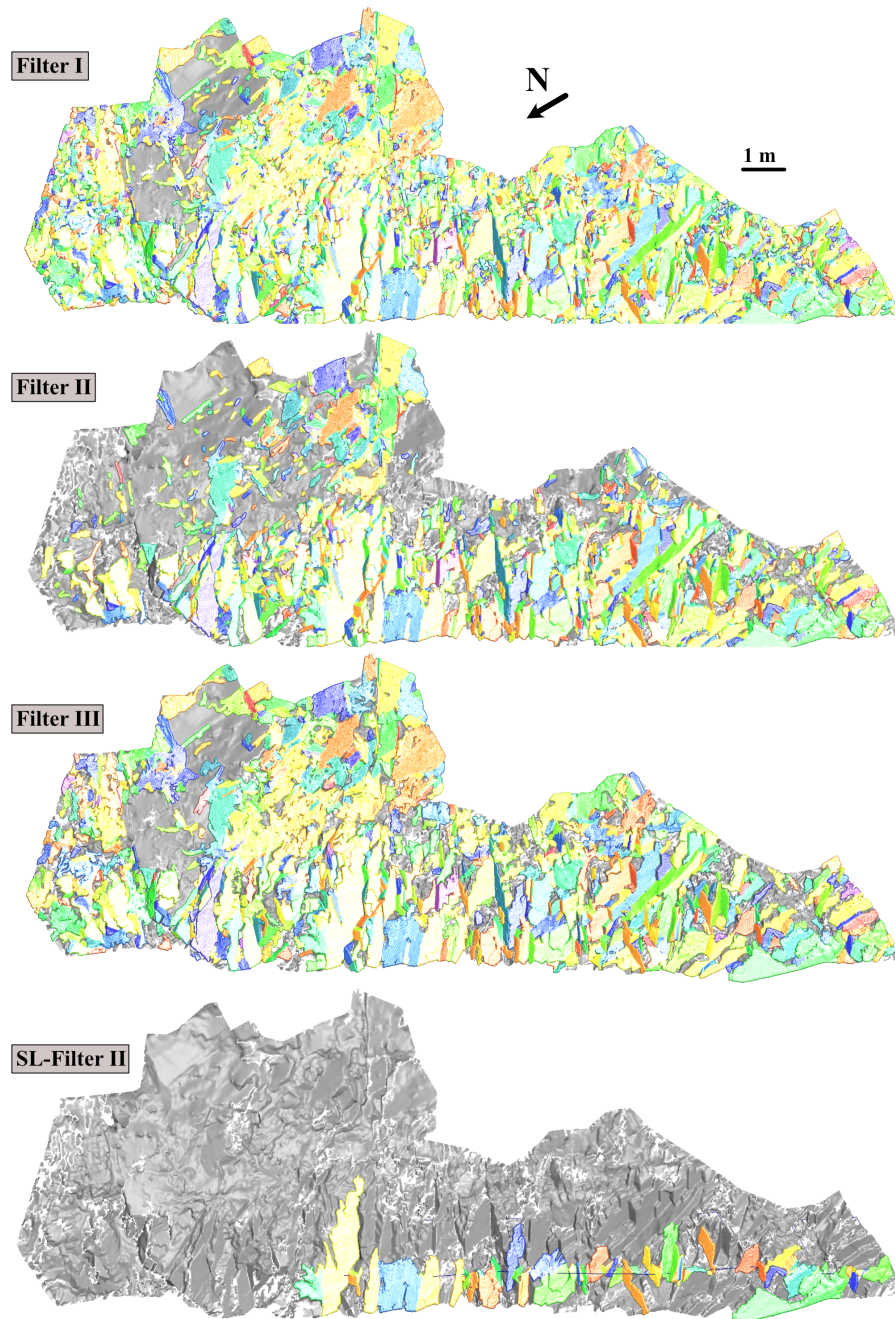


Figure B1. Picture of the fracture planes reconstruction (one colour = one fracture) from Combronde point cloud with filter I, II and III and the digital scan line extraction from filter I and II.

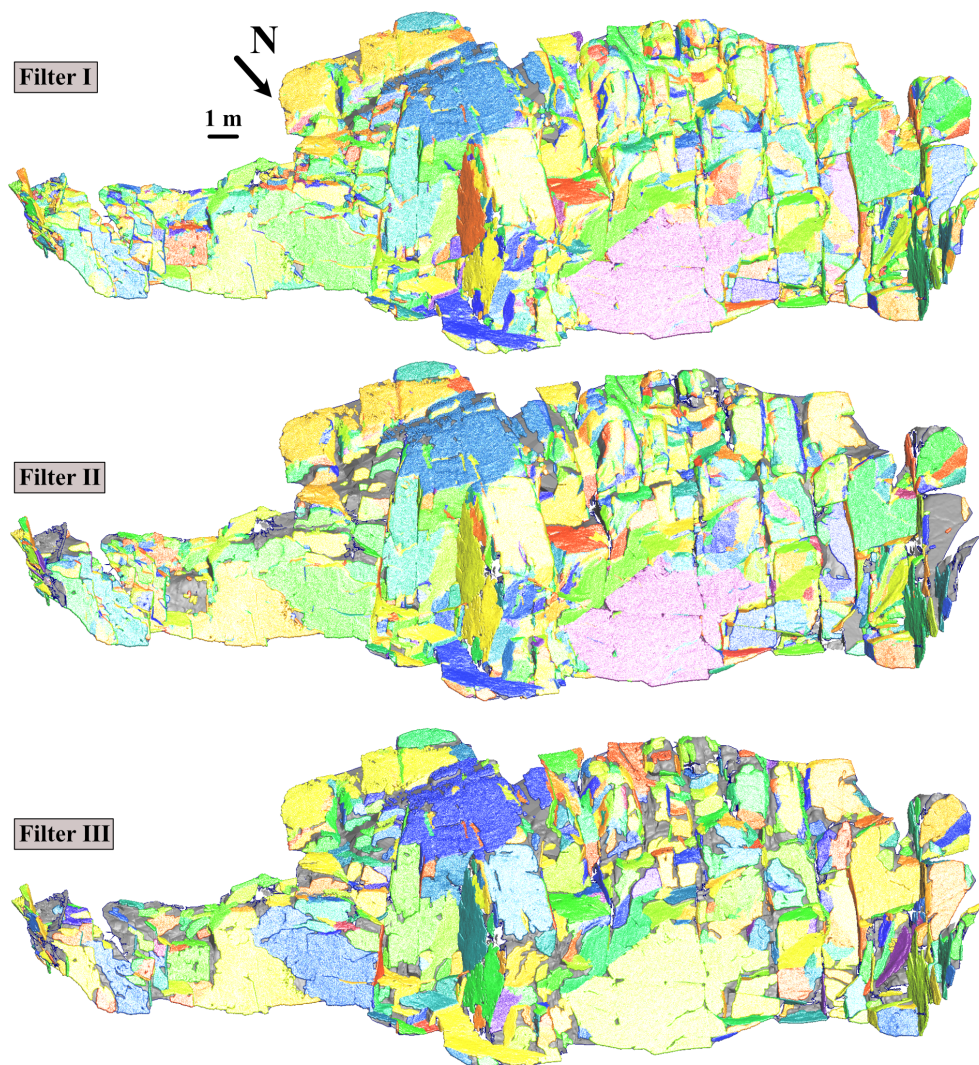


Figure C1. Picture of the fracture planes reconstruction (one colour = one fracture) from Tromm point cloud with filter I, II and III.

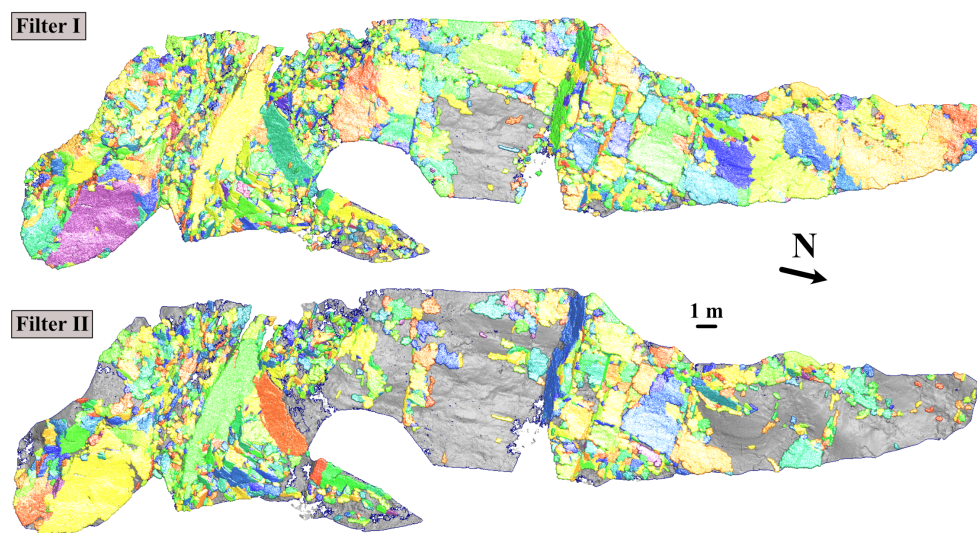


Figure D1. Picture of the fracture planes reconstruction (one colour = one fracture) from MULO point cloud with filter I and II.

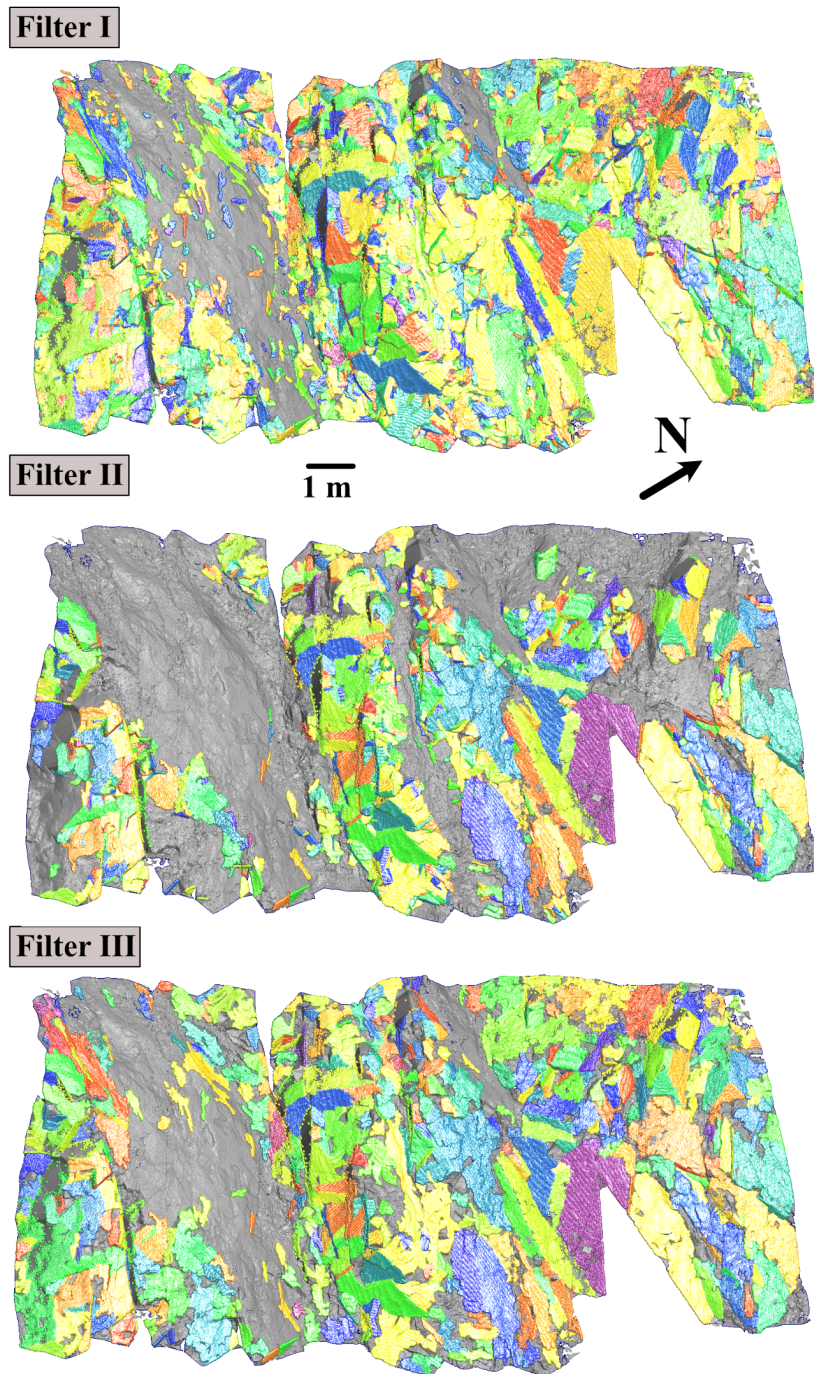


Figure E1. Picture of the fracture planes reconstruction (one colour = one fracture) from SC2 point cloud with filter I, II and III.



410 *Author contributions.* Dr. Lionel Bertrand has made the main part of the text and led the study. Dr. Claire Bossennec contributed with the geological aspects and results interpretation of the Odenwald outcrops. Dr. Wan-Chiu Li and Mr. Cédric Borgese wrote the description of the surface reconstruction and fracture plane recognition and the related results of this part of the workflow. Dr. Bruno Gavazzi add the P10, P21 and P32 computation methodology. Mr. Matthis Frey, Pr. Yves Géraud, Dr. Marc Diraison and Pr. Ingo Sass all together contributed to the scientific review of the results and discussion and english corrections.

415 *Competing interests.* The authors declare no conflict of interest. The funders had no role in the design of the study, in the collection, analyses, or interpretation of data, in the writing of the manuscript, or in the decision to publish the results.

420 *Disclaimer.* This research was supported by the BPI fund for the tool development and the Interreg NWE Programme for the dataset acquisition through the Roll-out of Deep Geothermal Energy in North-West Europe (DGE-ROLLOUT) Project (www.nweurope.eu/DGE-ROLLOUT) and also the REFLET Research program for the data in the Limagne area. The Interreg NWE Programme is part of the European Cohesion Policy and is financed by the European Regional Development Funds (ERDF). We acknowledge the support of the APC by the Deutsche Forschungsgemeinschaft (DFG – German Research Foundation) and the Open Access Publishing Fund of the Technical University of Darmstadt.

425 *Acknowledgements.* We would like to thank the HLNUG who provided digital elevation data, Sebastian Schröder and the municipalities of Wald-Michelbach and Rimbach for giving us access to the quarries in the Tromm Granite. We also would like to thank the Mitteldeutsche Hartstein-Industrie AG for granting access to the Mainzer Berg and Mühlthal quarry. RÖHRIGgranit GmbH is thanked for granting us access to their quarries in Heppenheim. We also would like to thank BPI France for their support of the tool development.



References

- Aubert, M., Bouiller, R., Camus, G., Cochet, A., D'Arcy, D., Giot, D., Jeambrun, M., Roche, A., and Bonhommet, N.: Carte géologique à 1/50000 de Clermont Ferrand, 1973.
- Barathon, J.-J.: Carte géologique Le Mayet-de-Montagne, Norois, 103, 439–439, 1979.
- 430 Bemis, S. P., Micklethwaite, S., Turner, D., James, M. R., Akciz, S., Thiele, S. T., and Bangash, H. A.: Ground-based and UAV-Based photogrammetry: A multi-scale, high-resolution mapping tool for structural geology and paleoseismology, *Journal of Structural Geology*, 69, 163–178, 2014.
- Bertrand, L., Geraud, Y., and Diraison, M.: Petrophysical properties in faulted basement rocks: Insights from outcropping analogues on the West European Rift shoulders, *Geothermics*, 95, 102–144, 2021.
- 435 Boltcheva, D. and Lévy, B.: Simple and Scalable Surface Reconstruction, Research report, LORIA - Université de Lorraine ; INRIA Nancy, <https://hal.science/hal-01349023>, 2016.
- Bonilla-Sierra, V., Elmouttie, M., Donzé, F.-V., and Scholtes, L.: Composite wedge failure using photogrammetric measurements and DFN-DEM modelling, *Journal of Rock Mechanics and Geotechnical Engineering*, 9, 41–53, 2017.
- Bonnet, E., Bour, O., Odling, N. E., Davy, P., Main, I., Cowie, P., and Berkowitz, B.: Scaling of fracture systems in geological media, *Reviews of Geophysics*, 39, 347–383, <https://doi.org/https://doi.org/10.1029/1999RG000074>, 2001.
- 440 Bossennec, C., Frey, M., Seib, L., Bär, K., and Sass, I.: Multiscale Characterisation of Fracture Patterns of a Crystalline Reservoir Analogue, *Geosciences*, 11, 371, 2021.
- Bossennec, C., Seib, L., Frey, M., van der Vaart, J., and Sass, I.: Structural Architecture and Permeability Patterns of Crystalline Reservoir Rocks in the Northern Upper Rhine Graben: Insights from Surface Analogues of the Odenwald, *Energies*, 15, 1310, 2022.
- 445 Bouillet, R., Giot, D., and Jeambrun, M.: Carte Géologique Thiers XXVI-31, à l'échelle 1: 50,000, Bureau de Recherches Géologiques et Minières, Orléans, 1972.
- Bourgeois, O., Ford, M., Diraison, M., Veslud, C., Gerbault, M., Pik, R., Ruby, N., and Bonnet, S.: Separation of rifting and lithospheric folding signatures in the NW-Alpine foreland, *International Journal of Earth Sciences*, 96, 1003–1031, 2007.
- Bourquin, S., Durand, M., Diez, J., Broutin, J., Fluteau, F., et al.: The Permian-Triassic boundary and Early Triassic sedimentation in Western European basins: an overview, *Journal of Iberian Geology*, 33, 221–236, 2007.
- 450 Bruguier, O., Becq-Giraudon, J., Bosch, D., and Lancelot, J.: Late Viséan hidden basins in the internal zones of the Variscan belt: U-Pb zircon evidence from the French Massif Central, *Geology*, 26, 627–630, 1998.
- Candela, T.: Roughness of fault surfaces: analyses and implications for the heterogeneity of seismic rupture, Ph.D. thesis, Université de Grenoble, 2011.
- 455 Cawood, A. J., Bond, C. E., Howell, J. A., Butler, R. W., and Totake, Y.: LiDAR, UAV or compass-clinometer? Accuracy, coverage and the effects on structural models, *Journal of Structural Geology*, 98, 67–82, 2017.
- Dadet, P., Vanitet, L., et al.: Carte géologique à 1/50000 de Maringues, 1980.
- Dashti, A., Gholami Korzani, M., Geuzaine, C., Egert, R., and Kohl, T.: Impact of structural uncertainty on tracer test design in faulted geothermal reservoirs, *Geothermics*, 107, 102–607, <https://doi.org/https://doi.org/10.1016/j.geothermics.2022.102607>, 2023.
- 460 Dershowitz, W.: Rock Joint Systems [Ph. D. thesis], Massachusetts Institute of Technology, Cambridge, 1984.



- Faure, M., Lardeaux, J.-M., and Ledru, P.: A review of the pre-Permian geology of the Variscan French Massif Central, *Comptes Rendus Geoscience*, 341, 202–213, <https://doi.org/https://doi.org/10.1016/j.crte.2008.12.001>, mécanique de l'orogénie varisque : Une vision moderne de la recherche dans le domaine de l'orogénie, 2009.
- 465 Frey, M., Bär, K., Stober, I., Reinecker, J., van der Vaart, J., and Sass, I.: Assessment of deep geothermal research and development in the Upper Rhine Graben, *Geothermal Energy*, 10, 1–67, 2022a.
- Frey, M., Bossennec, C., Seib, L., Bär, K., Schill, E., and Sass, I.: Interdisciplinary fracture network characterization in the crystalline basement: a case study from the Southern Odenwald, SW Germany, *Solid Earth*, 13, 935–955, 2022b.
- Hoppe, H.: Poisson surface reconstruction and its applications, p. 10, <https://doi.org/10.1145/1364901.1364904>, 2008.
- 470 Jacquemyn, C., Huysmans, M., Hunt, D., Casini, G., and Swennen, R.: Multi-scale three-dimensional distribution of fracture-and igneous intrusion-controlled hydrothermal dolomite from digital outcrop model, Latemar platform, Dolomites, northern Italy Three-dimensional Dolomite Distribution, *AAPG Bulletin*, 99, 957–984, 2015.
- La Pointe, P. R., Olofsson, I., and Hermanson, J.: Statistical model of fractures and deformations zones for Forsmark. Preliminary site description Forsmark area-version 1.2, 2005.
- 475 Lardeaux, J., Schulmann, K., Faure, M., Janoušek, V., Lexa, O., Skrzypek, E., Edel, J., and Štípská, P.: The moldanubian zone in the French Massif Central, Vosges/Schwarzwald and Bohemian Massif revisited: differences and similarities, *Geological Society, London, Special Publications*, 405, 7–44, 2014.
- Martinelli, M., Bistacchi, A., Mitterpergher, S., Bonneau, F., Balsamo, F., Caumon, G., and Meda, M.: Damage zone characterization combining scan-line and scan-area analysis on a km-scale Digital Outcrop Model: The Qala Fault (Gozo), *Journal of Structural Geology*, 140, 104 144, 2020.
- 480 Matte, P.: The Variscan collage and orogeny (480–290 Ma) and the tectonic definition of the Armorica microplate: a review, *Terra nova*, 13, 122–128, 2001.
- Micklethwaite, S., TURNER, D., VASUKI, Y., KoVESI, P., and Lucieer, A.: Mapping from an Armchair: Rapid, high-resolution mapping using UAV and computer vision technology, *Proceedings of Structural Geology and Resources*, pp. 130–133, 2012.
- Miernik, G. J.: TLS supported volumetric and DFN modeling of a fault zone in the Lower Buntsandstein, SW Germany, Ph.D. thesis, 2020.
- 485 Nance, R. D., Gutiérrez-Alonso, G., Keppie, J. D., Linnemann, U., Murphy, J. B., Quesada, C., Strachan, R. A., and Woodcock, N. H.: Evolution of the Rheic ocean, *Gondwana Research*, 17, 194–222, 2010.
- Nelson, R.: *Geologic analysis of naturally fractured reservoirs*, Elsevier, 2001.
- Niven, E. B. and Deutsch, C. V.: Relating Different Measures of Fracture Intensity, *CCG Annual Report-Paper 103*, 2010.
- Pauly, M., Gross, M., and Kobbelt, L.: Efficient simplification of point-sampled surfaces, *Visualization, 2002. VIS2002*, pp. 163–170, 2008.
- 490 Peacock, D., Nixon, C., Rotevatn, A., Sanderson, D., and Zuluaga, L.: Glossary of fault and other fracture networks, *Journal of Structural Geology*, 92, 12–29, 2016.
- Prabhakaran, R., Urai, J. L., Bertotti, G., Weismüller, C., and Smeulders, D. M.: Large-scale natural fracture network patterns: Insights from automated mapping in the Lilstock (Bristol Channel) limestone outcrops, *Journal of Structural Geology*, 150, 104 405, 2021.
- Schnabel, R., Wahl, R., and Klein, R.: RANSAC based out-of-core point-cloud shape detection for city-modeling, *Schriftenreihe des DVW, Terrestrisches Laser-Scanning (TLS 2007)*, 53, 2007.
- 495 Schumacher, M. E.: Upper Rhine Graben: role of preexisting structures during rift evolution, *Tectonics*, 21, 6–1, 2002.
- Seers, T. D. and Hodgetts, D.: Extraction of three-dimensional fracture trace maps from calibrated image sequences, *Geosphere*, 12, 1323–1340, 2016.



- Skrzypek, E., Schulmann, K., Tabaud, A.-S., and Edel, J.-B.: Palaeozoic evolution of the Variscan Vosges mountains, Geological Society, London, Special Publications, 405, 45–75, 2014.
- Slightam, C.: Characterizing seismic-scale faults pre-and post-drilling; Lewisian Basement, West of Shetlands, UK, Geological Society, London, Special Publications, 374, 311–331, 2014.
- Thews, J.-D.: Erläuterungen zur geologischen Übersichtskarte von Hessen 1: 300 000 (GÜK 300 Hessen).-T. 1. Kristallin, Ordoviz, Silur, Devon, Karbon, na, 1996.
- 505 Thiele, S. T., Grose, L., Samsu, A., Micklethwaite, S., Vollgger, S. A., and Cruden, A. R.: Rapid, semi-automatic fracture and contact mapping for point clouds, images and geophysical data, *Solid Earth*, 8, 1241–1253, 2017.
- van der Vaart, J., Bär, K., Frey, M., Reinecker, J., and Sass, I.: Quantifying model uncertainty of a geothermal 3D model of the Cenozoic deposits in the northern Upper Rhine Graben, Germany, *Zeitschrift der Deutschen Gesellschaft für Geowissenschaften*, 172, 365–379, <https://doi.org/10.1127/zdgg/2021/0286>, 2021.
- 510 Vazaios, I., Vlachopoulos, N., and Diederichs, M. S.: Integration of Lidar-based structural input and discrete fracture network generation for underground applications, *Geotechnical and Geological Engineering*, 35, 2227–2251, 2017.
- Wang, X.: Stereological interpretation of rock fracture traces on borehole walls and other cylindrical surfaces, Ph.D. thesis, Virginia Tech, 2005.
- Wang, X., Zou, L., Shen, X., Ren, Y., and Qin, Y.: A region-growing approach for automatic outcrop fracture extraction from a three-
- 515 dimensional point cloud, *Computers & Geosciences*, 99, <https://doi.org/10.1016/j.cageo.2016.11.002>, 2016.
- Ziegler, P.: Collision related intra-plate compression deformations in Western and Central Europe, *Journal of Geodynamics*, 11, 357–388, 1990.